



HAL
open science

Optimization of heteronuclear ultrafast 2D NMR for the study of complex mixtures hyperpolarized by dynamic nuclear polarization

Clément Praud, Victor Ribay, Arnab Dey, Benoît Charrier, Joris Mandral, Jonathan Farjon, Jean-Nicolas Dumez, Patrick Giraudeau

► To cite this version:

Clément Praud, Victor Ribay, Arnab Dey, Benoît Charrier, Joris Mandral, et al.. Optimization of heteronuclear ultrafast 2D NMR for the study of complex mixtures hyperpolarized by dynamic nuclear polarization. *Analytical Methods*, 2023, 15 (45), pp.6209-6219. 10.1039/D3AY01681A . hal-04309902

HAL Id: hal-04309902

<https://hal.science/hal-04309902>

Submitted on 30 Nov 2023

HAL is a multi-disciplinary open access archive for the deposit and dissemination of scientific research documents, whether they are published or not. The documents may come from teaching and research institutions in France or abroad, or from public or private research centers.

L'archive ouverte pluridisciplinaire **HAL**, est destinée au dépôt et à la diffusion de documents scientifiques de niveau recherche, publiés ou non, émanant des établissements d'enseignement et de recherche français ou étrangers, des laboratoires publics ou privés.

Optimization of heteronuclear ultrafast 2D NMR for the study of complex mixtures hyperpolarized by dynamic nuclear polarization

Clément Praud,^a Victor Ribay,^a Arnab Dey,^a Benoît Charrier,^a Joris Mandral,^a Jonathan Farjon,^a Jean-Nicolas Dumez^a and Patrick Giraudeau^{a*}

Received 00th January 20xx,
Accepted 00th January 20xx

DOI: 10.1039/x0xx00000x

Hyperpolarized ¹³C NMR at natural abundance, based on dissolution dynamic nuclear polarization (d-DNP), provides rich, sensitive and repeatable ¹³C NMR fingerprints of complex mixtures. However, the sensitivity enhancement is associated with challenges such as peak overlap and the difficulty to assign hyperpolarized ¹³C signals. Ultrafast (UF) 2D NMR spectroscopy makes it possible to record heteronuclear 2D maps of d-DNP hyperpolarized samples. Heteronuclear UF 2D NMR can provide correlation peaks that link quaternary carbons and protons through long-range scalar couplings. Here, we report the analytical assessment of an optimized UF long-range HETCOR pulse sequence, applied to the detection of metabolic mixtures at natural abundance hyperpolarized by d-DNP, based on repeatability and sensitivity considerations. We show that metabolite-dependent limits of quantification in the range of 1–50 mM (in the sample before dissolution) can be achieved, with a repeatability close to 10% and a very good linearity. We provide a detailed comparison of such analytical performance in two different dissolution solvents, D₂O and MeOD. The reported pulse sequence appears as a useful analytical tool to facilitate the assignment and integration of metabolite signals in hyperpolarized complex mixtures.

1. Introduction

Complex chemical mixtures can be defined as ensembles of molecules that coexist in a same matrix. Complexity can arise from the high number of coexisting components, the variety of chemical structures, the great diversity of concentrations, and potential chemical interactions. When such mixtures are studied by analytical methods, this chemical complexity can result in a challenging spectral complexity. Complex mixture analysis is a central topic in analytical chemistry and a challenge in a broad range of applications, such as “omic” sciences or reaction^{1–7} and process monitoring^{8–11}.

Several analytical tools can be used to get useful information on complex mixtures, such as Nuclear Magnetic Resonance Spectroscopy (NMR), Mass Spectrometry (MS) usually hyphenated with Liquid or Gas Chromatography (LC and GC respectively), infrared and Raman spectroscopies.^{12,13} NMR and MS methods are usually the most popular thanks to their ability to separate individual spectral patterns from mixture components. MS stands out with its unmatched sensitivity, but is limited by low repeatability and ambiguous signal assignments,^{1,14} while NMR can provide both structural and quantitative information in a robust and reproducible way with minimal sample preparation, but at the price of lower sensitivity and peak overlapping issues.¹⁵

Among NMR methods, 2D spectroscopy provides an efficient solution to the peak overlapping issue as it improves peak dispersion by spreading the chemical information over two orthogonal axes, thus helping signal assignment and compound identification.¹⁶ In metabolomics, 2D NMR can facilitate the separation of different sample classes after statistical analysis, as well as the identification of biomarkers.^{17,18} In reaction and process monitoring, 2D NMR

can also provide the peak separation needed to follow the concentration of individual mixture components over the course of time.¹⁹ The use of conventional 2D NMR for quantitative analysis, metabolomics and monitoring is limited by the long experiment durations needed to record enough t_1 increments to build the indirect dimension. However, the development of fast 2D NMR methods has enabled a number of applications in metabolomics and monitoring in the past few years, relying for instance on (i) fast pulse and optimized flip angles strategies (SOFAST, ALSOFAST, ASAP, VRT, etc.),^{20–22} (ii) alternative sampling strategies (NUS, Hadamard, etc.)^{23–25} or spatial parallelization methods.^{26,27}

A number of methods have been developed that brought major sensitivity improvements for the analysis of mixtures. Among them, Dynamic Nuclear Polarization (DNP) and Para-Hydrogen Induced Polarization (PHIP) appear to be the most widely used hyperpolarization techniques in analytical chemistry. PHIP consists of a catalytic hydrogenation reaction between an unsaturated molecule and hydrogen gas enriched in its para form (p -H₂), which results in a significant sensitivity enhancement. It can also be applied in a reversible way with Signal Amplification by Reversible Exchange polarization (SABRE) or non-hydrogenative PHIP (nh-PHIP).^{28–31} The latter has enabled quantitative 2D NMR applications on complex mixtures.^{32,33} PHIP methods are chemically selective, as only a few functional groups can bind to the organometallic complex.

DNP consists of transferring the high spin polarization of electrons to nuclear spins. It requires irradiating the sample with microwaves, in the presence of free electrons (typically those of radical molecules added to the sample). DNP allows a sensitivity enhancement of several orders of magnitude, in a non-selective way, which makes DNP a general hyperpolarization technique.³⁴ While the DNP process is mostly efficient at cryogenic temperatures and in the solid state, the dissolution-DNP (d-DNP) experiment enables detection of hyperpolarized signals in the liquid-state after subsequent dissolution of the hyperpolarized sample.³⁵

^aNantes Université, CNRS, CEISAM, UMR 6230, F-44000 Nantes, France

*patrick.giraudeau@univ-nantes.fr

Electronic Supplementary Information (ESI) available: [details of any supplementary information available should be included here]. See DOI: 10.1039/x0xx00000x

In the classic d-DNP workflow, (i) the sample is prepared in a so-called DNP juice (deuterated glycerol-water based solvent) with a stable radical (such as TEMPOL for instance) and (ii) frozen at cryogenic temperature, forming a glassy matrix inside a polarizer. (iii) The sample is then irradiated with microwaves at the electron resonance frequency to trigger specific electron-spin mechanisms in the solid state (dipole-dipole interaction and spin diffusion for instance), until the nuclear polarization build-up curve reaches its maximum. During this step, cross-polarization helps transferring the resulting ^1H polarization to less abundant nuclei such as ^{13}C .³⁶ (iv) A hot solvent is used to dissolve the hyperpolarized glassy matrix, and to transfer it into the nearby liquid-state spectrometer prior to its detection.^{35,37} Despite a general sensitivity gain of 4 orders of magnitude or more, d-DNP is limited by multiple factors.³⁸

The first limitation of d-DNP arises from polarization losses during the transfer time between the polarizer and the detection magnet. Once the sample reaches the liquid state, nuclei start to rapidly relax and the hyperpolarization decays according to the nuclear T_1 relaxation rates, which may be further reduced by the presence of radicals. This limits the range of nuclei that can be successfully detected after transferring the sample into the detection magnet. In the case of ^{13}C , d-DNP is best suited to detect quaternary ^{13}C nuclei thanks to their long T_1 relaxation rates. Many efforts have been devoted to the development of faster transfer methods, relying on gas- and liquid-driven injection.^{39–42} It has also been shown that a careful optimization of the d-DNP workflow allowed to reduce the transfer time while improving the analytical performances of the method.⁴³

In spite of this limitation, hyperpolarized 1D ^{13}C NMR has already found promising applications in metabolomics thanks to a very good repeatability.⁴⁴ It was applied to the analysis of metabolic fluxes on labelled cell and tissue extracts^{45–47} and also at natural ^{13}C abundance on plant extracts⁴⁸ or freeze-dried urine.⁴⁹ Despite very encouraging results, these studies also pointed out that direct ^{13}C detection with d-DNP lacked structural information, since peak assignment can be very challenging. Peak overlap is also an issue, due to the potentially very rich quaternary ^{13}C fingerprint in the 160–220 ppm range. This motivates the development of 2D NMR methods compatible with d-DNP, to study complex hyperpolarized metabolic mixtures.

Unfortunately, the second major limitation of d-DNP is the non-replenishable character of the resulting hyperpolarized signals, allowing only single-shot or small-angles strategies to record hyperpolarized spectra following dissolution and transfer. This limits drastically the use of conventional 2D NMR which needs several t_2 increments with comparable sensitivity to map the indirect dimension. A small-flip angle strategy has been applied with long-range HMBC (heteronuclear multiple bond correlation) to detect labelled hyperpolarized acetylated aminoacids found in blood serum.⁵⁰ A more general alternative relies on ultrafast (UF) 2D NMR spectroscopy. UF 2D NMR allows to record a 2D map in a single-scan fashion and in hundreds of milliseconds,⁵¹ which makes it a very promising candidate to be coupled with d-DNP.

The proof-of-concept of coupling d-DNP with UF 2D NMR was first reported in 2007⁵² and was followed by several investigations on model mixtures.^{53,54} In 2015, Dumez *et al.* used a UF pulse sequence to record UF heteronuclear 2D spectra on partially enriched and natural abundance breast cancer cell extracts.⁵⁵ A few homonuclear applications were also reported,^{56,57} but they require a short transfer time. Heteronuclear pulse sequences for d-DNP typically make use of the hyperpolarization of quaternary carbons, followed by a long-range coupling evolution period between quaternary ^{13}C and ^1H bonded in $^2J_{\text{CH}}$ and $^3J_{\text{CH}}$ and then by a coherence transfer from ^{13}C to ^1H prior to the detection. Indeed, quaternary ^{13}C have longer T_1 longitudinal relaxation times, which still provide, after the dissolution and transfer time, signal enhancements of 3 to 4 orders of magnitude. Moreover, many small molecules of interest such as metabolites possess at least a quaternary ^{13}C that makes them detectable with such pulse sequence. However, d-DNP UF 2D NMR is still at an early stage of development. In particular, the experiments reported above were recorded with triple-axis gradient probes that made it possible to perform coherence selection and spatial encoding on orthogonal axes.^{53,58} Moreover, the analytical performance of these methods has not been evaluated so far.

In this article, we investigate the analytical performance of an optimized heteronuclear UF pulse sequence, applied to a d-DNP workflow on natural abundance model mixtures. The reported pulse sequence aims at being applicable to a broad range of systems, and does not require specific hardware for the signal acquisition part. Repeatability and sensitivity assessments are provided at liquid state, through coefficient of variations (CV), linear regression and regression coefficient (R^2) and limit of quantification (LOQ). Pros and cons of the technique are discussed in light of future metabolomics applications.

2. Material and Methods

2.1. Chemicals

Deuterium oxide (D_2O , 99.9% D), deuterated methanol (CD_3OD , 99.9% D) and glycerol- d_8 (99% D) were purchased from Eurisotop (www.eurisotop.com). 4-hydroxy-2,2,6,6-tetramethylpiperidine-1-oxyl (4-hydroxy-TEMPO or TEMPOL) and sodium 3-trimethylsilylpropionate- d_4 (Na-TSP- d_4 ; 98% D) were obtained from Sigma-Aldrich (www.sigmaaldrich.com). All mentioned natural-abundance metabolites were all commercially available and were used as received unless otherwise noted.

2.2. Sample preparation

For d-DNP studies, a model metabolite mixture was prepared with raw powders of each of the ten following metabolites: L-alanine (Ala), sodium L-lactate (Lac), sodium pyruvate (Pyr), glycolic acid (Gly), succinic acid (Suc), L-arginine (Arg), citric acid (Cit), creatinine (Crea), γ -aminobutyric acid (GABA), sodium acetate (Ace), with TEMPOL at 50 mM. Metabolites used are shown in Fig. S1 in ESI. Weighted powders were dissolved in the classic DNP juice (glycerol- d_8 : D_2O :MilliQ water – 60:30:10 v/v)

to reach final individual metabolite concentrations of 200 mM. Then different stock solutions were prepared with the same 10 metabolites but with concentrations ranging from 20 to 160 mM, also dissolved with TEMPOL at 50 mM in DNP juice (the exact composition of each stock solution is available in Table S1 in the ESI). The 200 mM sample and the stock solutions with different metabolite concentrations were stored in several 250 μ L vials at -80 $^{\circ}$ C for at least one night. Prior to insertion of the sample in the polarizer, each vial spent about 10 minutes outside the fridge. The 1D 13 C reference spectrum of the hyperpolarized 200 mM 10-metabolite mixture is provided in Fig. 1.

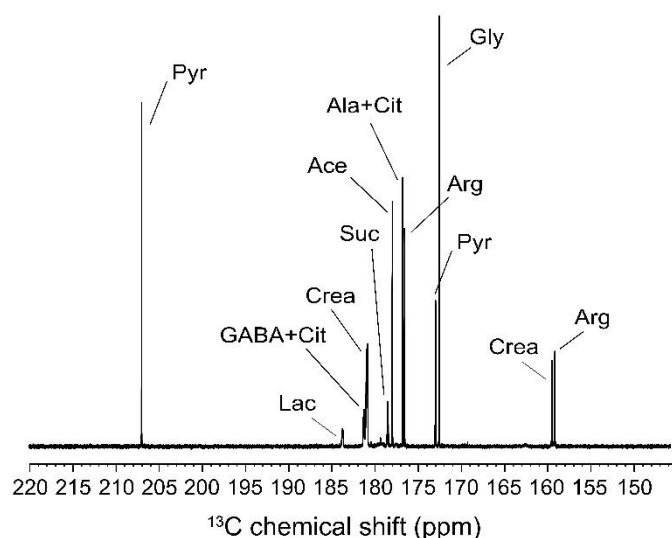


Fig. 1 13 C decoupled 1 H spectrum of a hyperpolarized 10-metabolite mixture at 200 mM (concentration before dissolution). The spectrum was recorded at 400 MHz, 298K and with a cryoprobe, after 21 minutes of hyperpolarization, 3.2 seconds of dissolution and transfer time and 8 seconds of stabilization, using D_2O as dissolution solvent. Arg: arginine; Crea: creatinine; Gly: glycolic acid; Pyr: pyruvate; Cit: citric acid; Ala: alanine; Suc: succinic acid; GABA: γ -aminobutyric acid; Lac: lactate. Signals were assigned using Table S2 provided in the ESI.

For conventional 2D HMBC experiments, two NMR tubes were prepared containing the 200 mM sample (described above) dissolved either in D_2O or MeOD for the second one, to reach 100 mM metabolite concentrations.

2.3 Apparatus

For d-DNP experiments, a prototype Bruker polarizer was used which enables solid-state DNP by combining a 7.05 T magnetic field, a cryostat to lower the sample temperature to 1.15 K, a microwave source, and a solid-state 1 H/ 13 C probe.

A 7.05 T wide-bore magnet was modified to accommodate a cryostat (Variable Temperature Insert, or VTI) consisting of two main parts: a phase separator (PS) and a space for sample polarization.

Liquid helium from a transport dewar is drawn at a controlled rate into the phase separator (PS) by a diaphragm vacuum pump (Vacuubrand MD 4 NT). The phase separator acts as a heat exchanger with baffles and radiation shields to cool the sample space. The evaporated helium is rejected by the

pump, and the liquid at the bottom of the PS is poured into the sample space via two automated needle valves. A main vacuum pump (Edwards iGx600L) connected to this space reduces the pressure to lower the temperature at 1.15 K. Numerous sensors measuring helium levels, temperatures, pressures and flow rates provide information to the Bruker software, for semi-automated control of the system, in interaction with the user. For the DNP experiment itself, a synthesizer generates a signal around 12 GHz, which then passes through an amplifier-multiplier chain (AMC, 16x frequency, Virginia Diodes), providing a microwave signal around 198 GHz, with an output power of 120 mW. A waveguide carries the microwaves to irradiate the sample. This signal is also software-controlled, with the option of TTL gating and applying different frequency modulations.

For solid-state NMR, a custom-built Bruker 1 H/ 13 C probe is located inside the cryostat, and can be manually matched and tuned from the outside. The overall circuit is able to achieve simultaneous nutation frequencies of 50 kHz without arcing. It is controlled by Topspin 4 and a NEO console.

The sample is contained in a PEEK cup screwed to the end of a 1.50 m long tube inserted manually into the cryostat so that the sample is at the centre of the NMR antennas and close to the output of the microwave waveguide.

The sample is dissolved by injecting (under helium gas pressure) a solvent (previously heated) through a capillary ending in a nozzle, which squirts onto the sample. Then the mixture rapidly liquefies and is pushed (by a \sim 9 bar pressure of He gas) into another outlet capillary towards the NMR spectrometer. The inlet and outlet capillaries are located in a stick which is manually inserted inside the tube supporting the sample cup. The output capillary part between the polarizer and the NMR spectrometer passes through a 0.8 T magnetic tunnel. Capillaries are 1.6 mm ID; The solvent heater is set at 170 $^{\circ}$ C and 12 bars for D_2O , and 156 $^{\circ}$ C and 16 bars for MeOD.

The conventional 5 mm NMR tube is fitted at the top with a passive injector open to atmospheric pressure and optimised so that the liquid (by gravity) flows through the tube with a minimum of turbulence.

The liquid-state NMR spectrometer is a 400 MHz Bruker Avance Neo, equipped with a nitrogen-cooled cryogenic probe (Prodigy, BBFO, ATMA, Z-gradient) and Topspin 4.

The polariser console is coupled to the 400 MHz spectrometer console to control the triggering of liquid NMR acquisition.

2.4 d-DNP Workflow

Once the sample, previously stored at -80° C, is ready (about 10 min at room temperature), 258 ± 2 mg of the sample are introduced in the DNP cup. The cup is then screwed at the bottom part of the sample stick. The sample space of the VTI is pressurised at 1200 mBar (above the atmosphere pressure) so that the top part of the VTI can be opened and the sample stick can be introduced completely. Then, the pressure is set to ramp down to 0.1 mBar. Once it is done, the PS needle valves are opened, so the liquid helium is poured in the sample space. When the VTI reaches 1.2 K, the pouring of liquid helium is

stopped and tuning and matching of the solid-state probe is performed.

The cross-polarization sequence is launched together with the microwave radiations to observe effective ^{13}C polarization building curve. Meantime, the dissolution box is filled with 5 mL of the desired solvent: D_2O or MeOD and then set at 170 or 156°C (with respect to the chosen solvent). After completion of the polarization, the sample stick is lifted by 10 cm and the dissolution stick is inserted within the sample stick. The dissolution is launched with a switch and the solvent rapidly melts the sample. Helium gas is used at 9.5 bars to push this liquid through the magnetic tunnel (0.56 T; DNP Instrumentation, <https://dnp-instrumentation.com/>), then into the injection device placed in the liquid-state NMR spectrometer until it fills completely the NMR tube. Thanks to an automatic trigger instruction programmed in the NMR pulse sequence, the acquisition starts to acquire signal after the end of the stabilization delay. NMR tubes are previously treated with Hellmanex® so the liquid can easily fill the NMR tube without creating too much bubbles (the Hellmanex® treatment is detailed in the ESI).⁴⁸

2.5 Solvent choice

Two solvents were tested for the dissolution step: D_2O and MeOD. These two solvents have different behaviours during dissolution, due to different chemical properties: (i) the studied metabolites are more soluble in D_2O than in MeOD, and (ii) the heat capacity is higher for MeOD (44 and 60 $\text{J}\cdot\text{mol}^{-1}\cdot\text{K}^{-1}$ at 298 and 500 K) than for D_2O (34 and 37 $\text{J}\cdot\text{mol}^{-1}\cdot\text{K}^{-1}$ at 298 and 500 K). It is important to note that the choice of the set temperature (at 156°C the pressure box rises to about 16 bars) for MeOD is limited by the pressure limit of the dissolution box (*ca.* 16 bars). Therefore, the D_2O set temperature is higher compared to MeOD (170°C for D_2O and only 156°C for MeOD). (iii) the surface tension of the liquid entering in the NMR tube is higher for D_2O than for MeOD. As a consequence, the risk of erratic motion in the NMR tube or of bubble formation is higher than with D_2O than MeOD. The last point is crucial concerning UF experiments, because the encoding and detection block are really sensitive to the sample instability induced by the rapid motion. As a consequence, the stabilization delay in D_2O is always higher than in MeOD, to deal with the more important convection and turbulences.

2.6 NMR acquisition parameters

The UF long-range HETCOR pulse sequence described in Fig. 2, was optimized to observe ^{13}C - ^1H correlations involving quaternary carbons. The start of the pulse sequence is triggered by the dissolution, after ~20 min of hyperpolarization and 3.2 s of dissolution and transfer delay. An optimised stabilization delay (SD) is placed at the start of the pulse sequence, and followed by a ^1H 90° and a 5 ms spoiler gradient of 42.8 G/cm, to dephase magnetizations arising from ^1H . After a 200 ms delay, a ^{13}C 90° pulse is applied to excite the hyperpolarized ^{13}C magnetization, followed by a long-range coupling delay (τ) of

33.57 ms which is optimized to observe $^2J_{\text{CH}}$ and $^3J_{\text{CH}}$ correlations. The spatial encoding block is composed of 4 chirp pulses with a duration of 5 ms and a sweep range of 30 kHz each, paired with encoding gradient of ± 2.79 G/cm. It leads to an effective encoding time of less than 5 ms, which results in peak broadening effects (as shown latter in Fig. 3). The second and fourth chirp pulses are flanked by spoiler gradients of amplitude 44.66 G/cm and duration 1.2 ms. The central ^1H 180° pulse and optimized delays (t_{sym}) on both sides of this pulse allow to refocus undesired J -coupling evolution. Coherence-selection gradients G_1 (- 44.66 G/cm) and G_2 (+ 11.16 G/cm) flank the 90° $^{13}\text{C}\rightarrow^1\text{H}$ coherence transfer pulses. A pre-acquisition gradient of - 22.33 G/cm is followed by an EPSI block composed of 128 pairs of gradients of amplitude ± 44.66 G/cm and duration 270 μs each. The α constant of 1.0003 is used to multiply the second gradient amplitude in each EPSI loop to compensate for gradient imbalance and ensure linear echo trajectories in the (k , t_2) domain. Offsets of 2.5 ppm (^1H) and 175 ppm (^{13}C) were chosen to map the ^{13}C quaternary region, and spectral widths of 4.2 x 90 ppm were achieved in the ^1H (conventional) and ^{13}C (ultrafast) dimensions respectively.

In addition to UF hyperpolarized experiments, two conventional HMBC spectra were recorded, one for each two tubes, during 3 hours (512 t_1 increments and 4 scans), providing 220 x 5 ppm 2D maps. The acquisition time was set to 1.024 s, followed by a 1.5 s delay before the next transient for ^1H nuclei relaxation. Low-pass J -filters were applied to suppress one-bond coupling correlations (120-170 Hz) and no decoupling was used during the acquisition.

2.7 NMR processing parameters

Conventional 2D HMBC experiments were processed in Topspin. 2D FIDs were apodised with sine shape functions, zero-filled to 2048 in F2 and 2048 in F1 and Fourier transformed. Spectra were displayed in magnitude mode.

UF 2D experiments were processed using a custom MATLAB code. FIDs were imported in MATLAB and then rearranged into 2D matrices. Data acquired from positive and negative gradients were split in two subsets, processed separately and then co-added after a shift correction between the two subsets. Along the spatial dimension, data were submitted to inverse Fourier transformation, then apodised by a Gaussian shape function in the spatial domain, zero-filled to 1024 points and Fourier transformed. Along the spectral dimension, data were apodised with a sine shape function, zero-filled to 1024 points and Fourier transformed. Spectra were then plotted in magnitude mode.

Peak picking was performed on resulting spectra with custom MATLAB code, to select signal, noise and artefact 2D regions. Still with a custom MATLAB code, integrals were measured for each signal as the sum of intensities in the selected 2D region, and SNR was calculated as the ratio of the maximum signal intensity over the mean statistical noise of the 2D noise region.

3. Results and discussion

3.1. Analysis of UF 2D spectra

The ultrafast long-range pulse sequence in Fig. 2 was implemented and optimized to observe long-range correlation peaks involving quaternary carbons and protons that are separated by 2 or 3 bonds ($^2J_{CH}$ or $^3J_{CH}$ couplings). While this

approach has already been suggested to record UF 2D spectra after d-DNP,^{53,54} the coherence selection and spatial encoding gradient schemes in Fig. 2 were carefully optimized using gradients on a single axis. Indeed, our system is not equipped with a triple-axis gradient probe, as we aimed at designing a general pulse sequence applicable to a standard system.

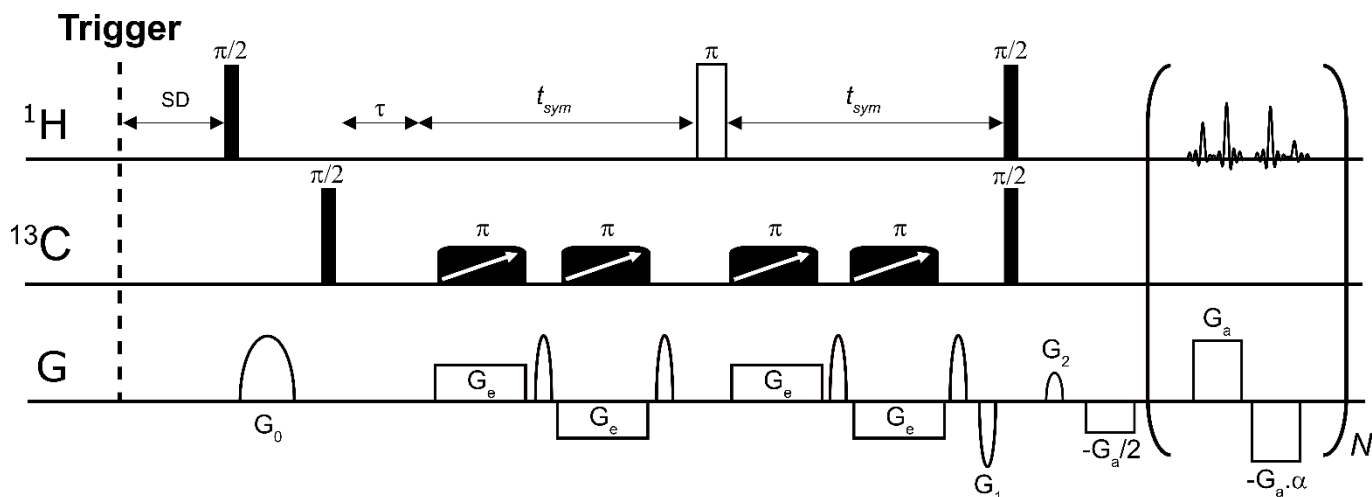


Fig. 2 UF long-range HETCOR pulse sequence scheme. SD is the delay for stabilization of the sample in the NMR tube after injection. Proton saturation is performed prior to ^{13}C excitation. τ allows to select coherences from $^3J_{CH}$ and $^2J_{CH}$ involving ^1H bonded to quaternary ^{13}C . A four-chirp encoding scheme is used and J -coupling evolution during this period is carefully controlled by t_{sym} delays. G_1 and G_2 are the selection coherence gradients used to select the wanted coherence pathway, and $G_1/G_2 = \gamma(^1\text{H})/\gamma(^{13}\text{C})$. The second EPSI gradient is multiplied by a constant α to correct the echoes linearity during the EPSI train. The dotted line at the beginning of the pulse sequence refers to the TTL trigger activation, allowing to start the experiment after the sample injection in the NMR tube

Conventional HMBC and d-DNP UF 2D spectra, obtained on a model mixture of 10 metabolites, are shown in Fig. 3. Hyperpolarized spectra obtained in a single scan after dissolution in two different dissolution solvents (Fig. 3b and "c") are compared to a conventional HMBC experiment recorded in D_2O in 3 h (Fig. 3a). For d-DNP UF 2D experiments, each metabolite has a concentration of 200 mM in the sample cup and around 2 mM after dissolution in the NMR tube, while each metabolite is at 100 mM for the conventional HMBC experiment. The corresponding peak assignments are provided in Table S2 in the ESI. The UF spectrum recorded in D_2O after d-DNP (Fig. 3b) shows a number of correlation peaks that are in good agreement with the reference HMBC spectrum (Fig. 3a). This illustrates the ability of the d-DNP UF 2D NMR to provide relevant chemical-shift information. Note that within the same experiment time, it is possible to record a non-hyperpolarized IMPACT-HMBC spectrum on the same sample (Fig. S2 in the ESI), provided that time-saving strategies are implemented.⁵⁹ However, such experiment has its own drawbacks and challenges such as NUS artefacts for instance (see Fig. S2 in the ESI). Moreover, being recorded on a thermally polarized sample, this approach would not help to accurately assign hyperpolarized post-dissolution ^{13}C signals. One should also notice that compared to the 1D ^{13}C hyperpolarized spectrum showed in Fig. 1, the peak dispersion provided by UF 2D spectroscopy allows to better separate individual signals.

Individual signal enhancements were not calculated here, but typical enhancement values obtained on this experimental setup can be found in the literature.⁴³

The main differences between conventional and UF experiments is the resolution penalty in the ^{13}C dimension of the UF spectrum, and the large ridges along the ^{13}C dimension between 3.9 and 3.5 ppm that are clearly visible in Fig. 3b. The former difference is due to the spectral width/resolution compromise inherent to UF 2D NMR.⁶⁰ When multiple scans can be recorded, this compromise can be addressed through interleaved experiment, an option that was not possible here due to the non-replenishable nature of hyperpolarization. Therefore, we chose to reduce the effective evolution time in the indirect dimension so that all relevant ^{13}C resonances can be detected in a single scan (see section 2.6.). The noise ridges along the ^{13}C dimension are mainly due to the strong residual motion (turbulences) occurring after dissolution, which result in unwanted magnetizations which are not completely suppressed by the coherence selection scheme. Such noise ridges can prevent the correct observation of less sensitive correlations. Five peaks over the 18 expected are discarded in Fig. 3b (peaks labelled 8, 11, 13, 16 and 18 in the conventional HMBC), as their SNR in the ultrafast dimension is below the limit of detection ($\text{SNR} < 3$), and 4 peaks over 18 in Fig. 3c (peaks labelled 3, 8, 12 and 14).

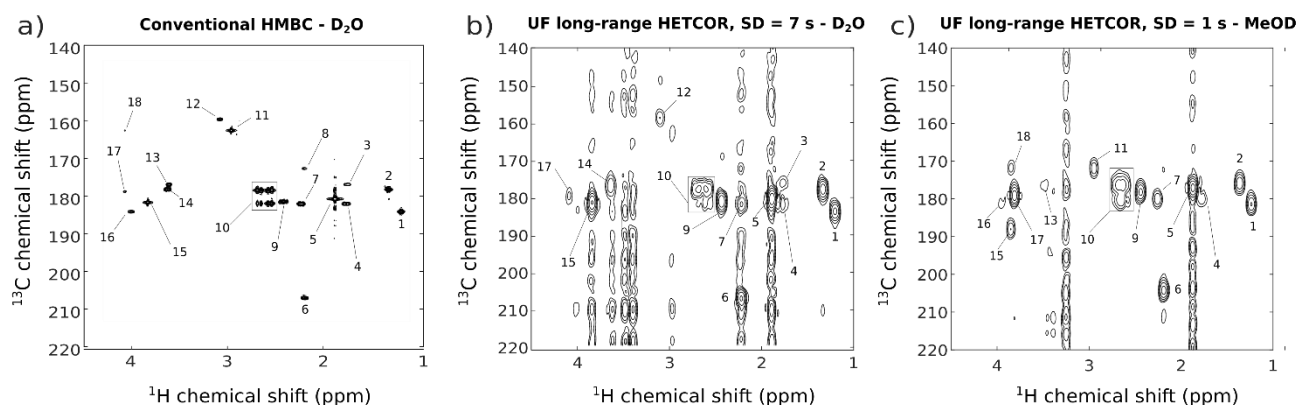


Fig. 3 Heteronuclear 2D spectra of a model metabolite mixture at natural ^{13}C abundance recorded at 400 MHz. (a) Reference spectrum acquired with a conventional HMBC pulse sequence in 3 hours with 4 scans and 512 t_1 increments; (b) UF long-range HETCOR spectrum recorded in a single scan and in D_2O after 20 minutes of hyperpolarization, 3.2 seconds of transfer and 7 seconds of stabilization; (c) UF long-range HETCOR spectrum recorded in a single scan and in MeOD after 21 minutes of hyperpolarization, 3.2 seconds of transfer and 1 second of stabilization. 1: Lac $^3J_{\text{CH}}$; 2: Ala $^3J_{\text{CH}}$; 3: Arg $^3J_{\text{CH}}$; 4: GABA $^3J_{\text{CH}}$; 5: Ace $^2J_{\text{CH}}$; 6: Pyr $^3J_{\text{CH}}$; 7: GABA $^2J_{\text{CH}}$; 8: Pyr $^2J_{\text{CH}}$; 9: Suc $^2J_{\text{CH}}$ and $^3J_{\text{CH}}$; 10: Cit: $^2J_{\text{CH}}$ and $^3J_{\text{CH}}$; 11: Crea $^3J_{\text{CH}}$; 12: Arg $^3J_{\text{CH}}$; 13: Ala $^2J_{\text{CH}}$; 14: Arg $^2J_{\text{CH}}$; 15: Crea $^2J_{\text{CH}}$; 16: Lac $^2J_{\text{CH}}$; 17: Gly $^2J_{\text{CH}}$; 18: Crea $^3J_{\text{CH}}$. Complete peak assignment table is provided in Table S2 in ESI. Spectra were recorded on a 400 MHz spectrometer equipped with a BBO prodigy at 298 K for D_2O experiments and at 293 K for MeOD experiment.

Such noise ridges could be minimized by the use of triple-axis gradient probes that would allow to perform coherence selection and spatial encoding on orthogonal axes.^{53,58} Similar conclusions can be drawn by comparing the UF spectrum obtained after dissolution in MeOD (Fig. 3c) with its conventional HMBC counterpart (Fig. S3). Differences are also observed between the two UF spectra, as could be expected from the use of a different solvent which impacts both the metabolite signals (concentration and chemical shift) and the residual solvent magnetization.

3.2. Stabilization delay and repeatability

In Fig. 3, UF spectra reported for the two dissolution solvents were recorded with different stabilization delays. In fact, the

choice of the optimum stabilization delay (SD) is a compromise between the need to reduce the impact of residual sample motion after dissolution, and the polarisation decay when SD increases. Careful optimization of this delay is shown in Fig. 4 for dissolution in D_2O (only three delays are shown here but additional spectra are shown in Fig. S4 in the ESI). The spectra recorded with increasing values of SD clearly show that noise ridges arising from residual sample motion decrease when SD increases, albeit at the cost of a sensitivity penalty for metabolite peaks due to the polarization decay. Note that SD values shorter than 6 seconds were also evaluated but showed even more intense noise ridges, making it difficult to detect metabolite signals.

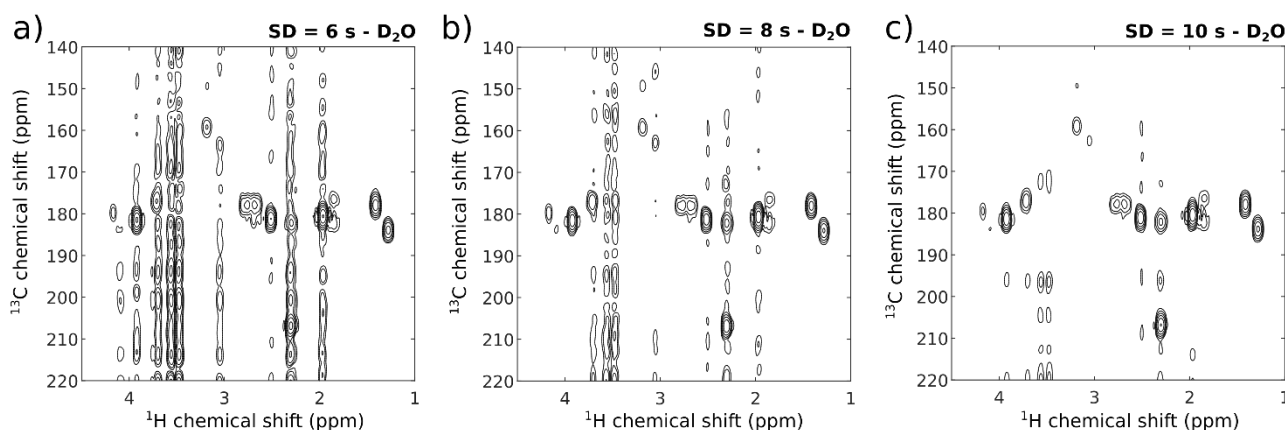


Fig. 4 UF long-range HETCOR spectra recorded after 21 minutes of hyperpolarization, 3.2 seconds of transfer and 6 (a), 8 (b) and 10 (c) seconds of stabilization delay respectively. Each experiment was recorded after a dissolution in D_2O solvent, on a 400 MHz spectrometer equipped with a BBO prodigy at 298 K.

Fig. 5 shows analytical data for the all the reported signals (cf. Fig. 3b), obtained from triplicate experiments with different SD values after dissolution in D_2O . The coefficients of variation of

2D peak volumes (normalized to the alanine signal, as it is well resolved, not overlapped and not affected by a ridge artefact) show optimum values for a SD of 6 s (with an average CV of

11.95% and 10.05% without accounting for Cit (10) CV%) and 7 s (with an average CV of 13.33% and 8.65%). Fig. 5b shows that SD = 7 s provides a slightly higher 2D SNR in average, with more accuracy on the 2D SNR measurement. Note that this graph also shows a peak-dependent sensitivity, which is further discussed in section 3.3.3. Overall, these results indicate that SD = 7 s is an optimum value for dissolution in D₂O with our experimental

setting. The triplicate spectra obtained at SD = 7 seconds are shown in Fig. S5 in the ESI.

The same study was conducted for d-DNP UF 2D experiments with MeOD as dissolution solvent, and shorter stabilization delays of 1, 2 and 3 seconds were tested 3 times. Corresponding UF spectra for each tested SD are available in Fig. S6 in the ESI and give rise to similar observations and conclusions as for D₂O experiments.

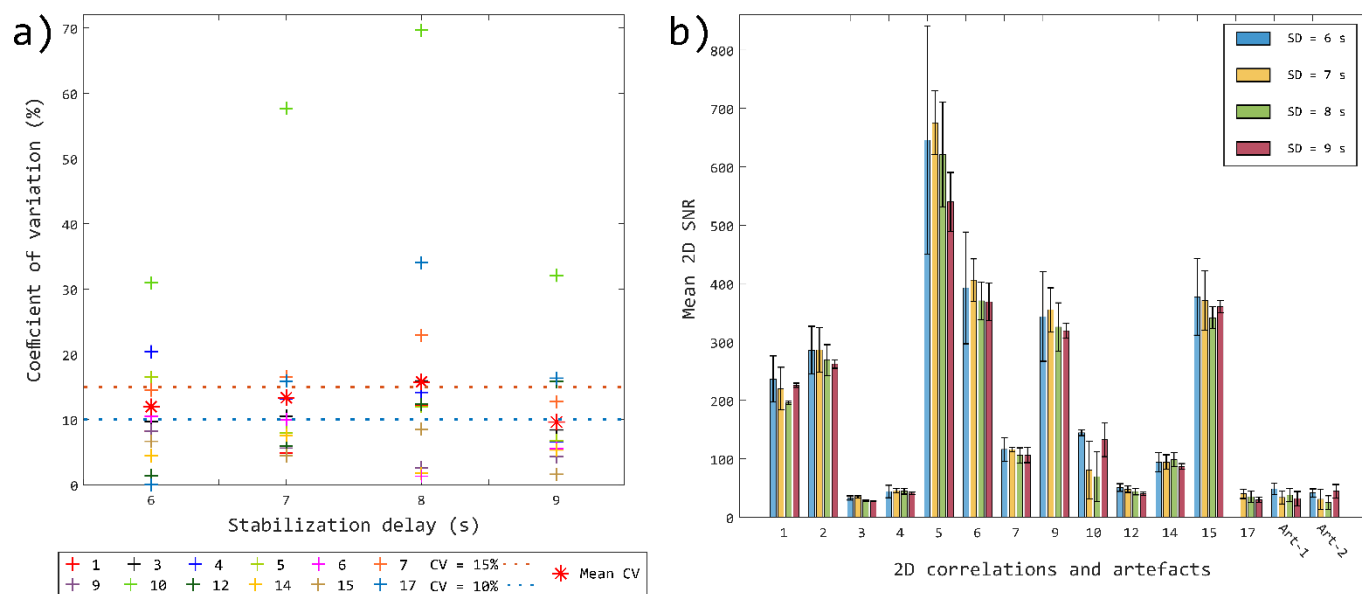


Fig. 5 (a) Coefficients of variation on 2D peak integrals calculated on 3 replicates for 12 different sites among 9 metabolites (Lac (1), Arg (3), (12) and (14), GABA (4) and (7), Ace (5), Pyr (6), Suc (9), Cit (10), Crea (15) and Gly (17)), with respect to the chosen stabilization delay (SD) for D₂O dissolutions. Blue and orange dotted lines correspond respectively to CV of 10 and 15%. Red star symbols correspond to the mean CV measured for each stabilization delay. Coefficient of variations were calculated from 2D peak volume integrals normalized to the alanine Ala (2) peak volume. (b) Average 2D SNR calculated on 3 replicates for 10 different metabolite signals (Lac (1), Ala (2), Arg (3), (12) and (14), GABA (4) and (7), Ace (5), Pyr (6), Suc (9), Cit (10), Crea (15) and Gly (17)) and after a different stabilization delay for D₂O dissolutions. Error bars correspond to the measured standard deviation on 2D SNR for each 3 replicates. Artefacts 1 and 2 bars corresponds to the maximum signal of a ridge divided by the mean noise. Art-1 corresponds to the spreading artefacts located between 3.9 and 3.5 ppm and Art-2, to the artefacts between 2.5 and 2.0 ppm. Data for SD = 10 s were not analysed because of an experimental failure on one of the replicates.

As reported earlier,⁴³ shorter SD values are allowed with MeOD because it has a less turbulent behaviour, thanks to a lower viscosity and surface tension compared to D₂O. Fig. 6a shows

that the CV of the 2D peak volumes (normalized to the alanine site) for SD of 1 and 2 seconds are better in most cases (mean CV = 12.48% at SD = 1 s and 10.22% at SD = 2 s).

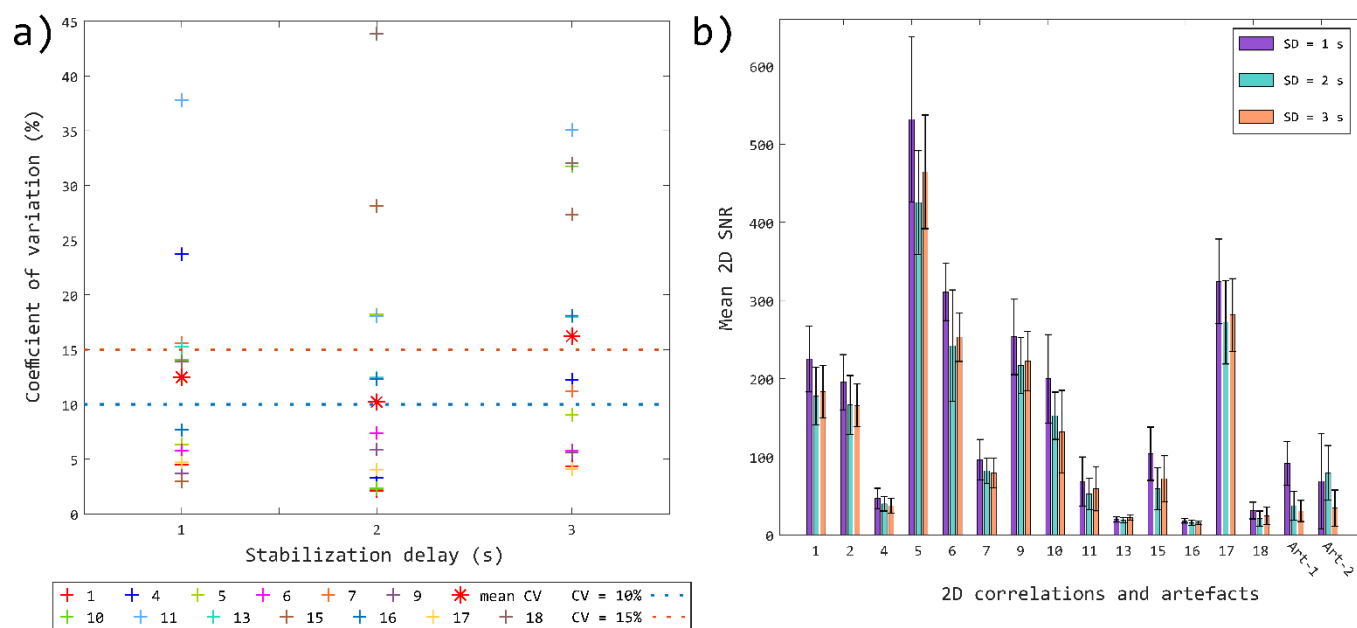


Fig. 6 (a) Coefficients of variation calculated on 3 replicates for 13 different sites among 9 metabolites (Lac (1) and (16), GABA (4) and (7), Ace (5), Pyr (6), Suc (9), Cit (10), Crea (11), (15) and (18), Ala (13) and Gly (17)), with respect to the chosen stabilization delay (SD) for MeOD dissolutions. Blue and orange dotted lines correspond respectively to CV of 10 and 15. Red star symbols corresponds to the mean CV measured for each stabilization delay. Coefficient of variations were from 2D peak volume integrals normalized to the alanine peak volume. (b) Average 2D SNR calculated on 3 replicates for 14 different sites among 10 metabolites (Lac (1) and (16), Ala (2) and (13), GABA (4) and (7), Ace (5), Pyr (6), Suc (9), Cit (10), Crea (11), (15) and (18), and Gly (17)) and after a different stabilization delay for MeOD dissolutions. Error bars correspond to the measured standard deviation for each 3 replicates. Artefacts 1 and 2 bars correspond to the maximum signal of a ridge artefact divided by the mean noise. Art-1 corresponds to the ridge artefacts located between 3.9 and 3.5 ppm and Art-2, to the artefacts between 2.5 and 2.0 ppm.

Fig. 6b highlights better 2D SNR at 1 second than for others SD for all signals. Therefore, the optimal SD for MeOD dissolutions is of 1 s in our experimental setting

Overall, stabilization delays of 7 and 1 s can be considered as optimal for dissolutions in D_2O and MeOD, respectively. Dissolutions performed in D_2O solvent give higher 2D SNR in average but at the cost of a higher CV% on 2D peak integrals than MeOD dissolutions. Even if the hyperpolarization losses are lower in MeOD due to a shorter SD, the higher SNR in D_2O can be attributed to the better solubility of metabolites in this solvent.

The lower MeOD dissolution efficiency was corroborated by 1D 1H thermal spectra, recorded at thermal equilibrium after dissolution in both solvents (a total of 6 spectra, 3 recorded in D_2O and 3 in MeOD, are shown in Fig. S7 in the ESI). 1D peak integrals are higher in D_2O , showing the better metabolite solubility in this solvent. The better repeatability of dissolutions in MeOD can be attributed to the less turbulent residual sample motion after dissolution. In addition, it should be mentioned that dissolutions in MeOD have a lower failure rate (5 to 10%, versus 15 to 20% in D_2O).

3.3. Linearity and limits of quantification

To evaluate the LOQ of the method, 5 stock solutions containing the same 10 metabolites as previously, but at concentrations ranging from 20 to 160 mM were prepared. Each stock solution contained the same total metabolite concentration to avoid co-solubility problems and to have similar ionic strength, but each metabolite was introduced at a different concentration in each

stock solution. After acquiring hyperpolarized 2D data on the different stock solutions, linear regressions of measured 2D SNR versus the concentration were plotted for each metabolite.

Example linear plots are shown in Fig. 7, for 4 metabolites: alanine, GABA, succinic acid and arginine after dissolutions performed in D_2O (data for other metabolites are provided in Fig. S8 in the ESI). Linear regression fits were performed on 4 points instead of 5, as one experiment failed at the detection stage, due to ice presence inside the polarizer. 2D SNR values measured from this one were largely biased for some metabolites, as shown by the red cross points in Fig. 7. Table 1 shows more detailed results for all the studied chemical sites, still in D_2O .

Based on Fig. 7, one can see that each 2D peak correlation gives a linear 2D SNR response, which is illustrated by the good regression coefficients highlighted in Fig. 7 and Table 1. An exception is creatinine which does not provide a linear fit as shown in Fig. S8. Despite the good 2D SNR and repeatability observed for this correlation (see Fig. 5), the potential chemical exchange with its creatine form at lower concentration prevents the linear response of creatinine, especially in D_2O , an effect which has also been described in conventional 1D NMR.⁶¹ Table 1 also shows the LOQ estimated using the linear regression equations, considering that a 2D SNR of 10 is the reasonable limit for a signal to be properly quantified.

The slope values are heterogenous among the different fitted metabolite 2D peaks (as discussed in section 3.3.3). As a consequence, the estimated LOQ values shown in Table 1 are also peak-dependent and comprised between 52 mM and 1.1

mM for respectively the least and the most sensitive 2D peak. A similar study of the analytical performance was carried out for dissolution in MeOD. Linear regressions graphs and parameters, and resulting limits of quantification are reported in ESI (Fig. S9 and Table S3).

Regression linearities in MeOD are more heterogeneous, as 6 2D correlations give $R^2 > 0.9$ (including 4 with $R^2 > 0.95$) over 10, while other 2D correlations show bad linearities. This can be explained by the presence of noise ridges arising from MeOD in the relevant chemical shift range.

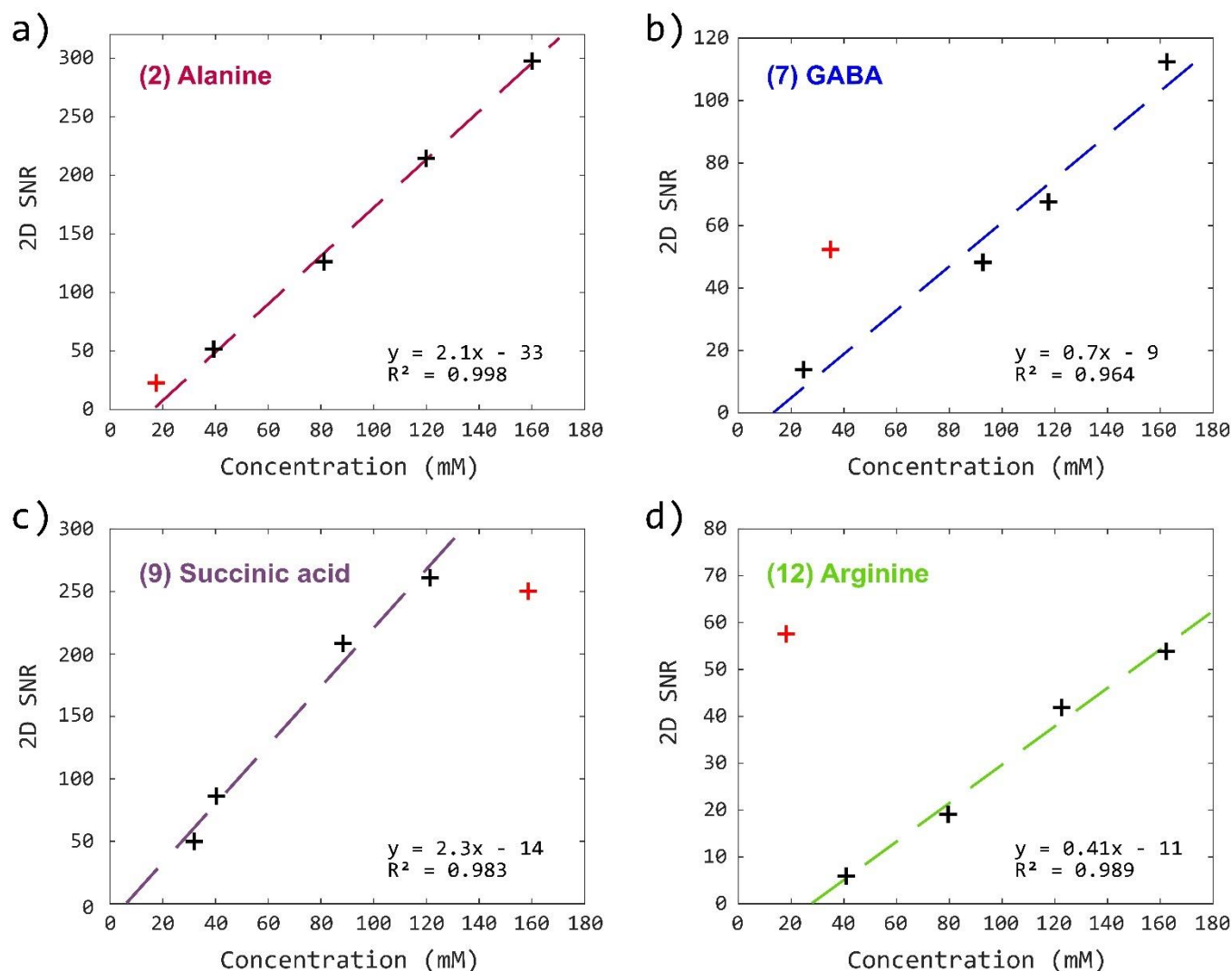


Fig. 7 Linear regressions of 4 different metabolite hyperpolarized 2D signals after dissolution in D_2O showing 2D SNR evolution with respect to the input concentration of each metabolite in mM. Regression equations and coefficients are shown. a) corresponds to the $^3J_{CH}$ correlation of alanine (2), b) to the $^3J_{CH}$ correlation of GABA (7), c) to the $^3J_{CH}$ correlation of succinic acid (9) and d) to the $^3J_{CH}$ correlation of arginine (12). 4 points were used to build the linear regressions, while one point (red cross) was discarded on each regression and corresponds to the LOQ4 experiment (cf. Table S1 in the ESI) that failed at the detection stage.

In order to check the repeatability close to the LOQ estimation, triplicate experiments were recorded on a 10-metabolites mixture at 25 mM each with 50 mM TEMPOL in DNP juice, in the case of dissolution in D_2O (cf. Fig. S10 in the ESI). 2D peak volumes, normalized to the alanine 2D peak volume, were used to determine the CV% of each 2D correlation. Results are

depicted in Table 2, and show average CV% of 13.1%, close to the CV% obtained from dissolution in D_2O of the 200 mM sample. These results show that the method remains repeatable even close to the limit of quantification, despite the presence of artefacts.

Table 1 Linear regression parameters and calculated LOQ for 9 chemical sites based on the measurement of 2D SNR as a function of concentration, after dissolutions performed in D₂O. LOQ is calculated by solving the linear regression equations with $\gamma = 10$ (approximation of the SNR value that should correspond to the lower concentration that can be quantified with the method). It corresponds to the minimal input concentration that can be prepared in the DNP cup to obtain an exploitable hyperpolarized 2D signal with SNR > 10. As creatinine $R^2 > 0.5$, regression results could not be interpreted and LOQ estimated (see Fig. S8 in the ESI).

Peak	Metabolite	Slope	y-intercept	R ²	LOQ _{calc} (input/ mM)
1	Lac (³ J _{CH})	1.7 ± 0.4	- 34 ± 42	0.910	26
2	Ala (³ J _{CH})	2.1 ± 0.1	33 ± 7	0.998	21
5	Ace (² J _{CH})	3 ± 1	13 ± 64	0.926	1.1
6	Pyr (² J _{CH})	2 ± 1	21 ± 64	0.892	5.1
7	GABA (² J _{CH})	0.7 ± 0.1	-9 ± 11	0.964	27
9	Suc (² J _{CH})	2.3 ± 0.2	-14 ± 17	0.983	10
12	Arg (³ J _{CH})	0.41 ± 0.03	- 11 ± 3	0.989	52
14	Arg (² J _{CH})	0.7 ± 0.2	- 7 ± 17	0.910	24
15	Crea (³ J _{CH})	N/A	N/A	N/A	N/A

Table 2 CV% on normalized 2D peak volumes for a 25 mM metabolite mixture after hyperpolarization and dissolution in D₂O, based on triplicate d-DNP UF 2D experiments. Each value represents the variation of the relative 2D peak integral normalized to the alanine peak.

Metabolites	Labels	CV%/D ₂ O solvent
Lactate (³ J _{CH})	(1)	14.6
Acetate (² J _{CH})	(5)	8.86
Pyruvate (² J _{CH})	(6)	20.5
GABA (² J _{CH})	(7)	14.2
Succinic Acid (² J _{CH})	(9)	15.3
Creatinine (³ J _{CH})	(11)	14.8
Creatinine (² J _{CH})	(15)	8.19
Lactate (² J _{CH})	(16)	8.94
Glycolic Acid (² J _{CH})	(17)	6.47
Creatinine (³ J _{CH})	(18)	11.8
	Mean CV%	13.1

3.6 Discussion

The results presented above show that the UF heteronuclear long-range pulse sequence has a good analytical performance for the analysis of metabolite mixtures at natural ¹³C abundance, with a repeatability of a few percent on normalized 2D peak integrals and limits of detection of a few tens of mM.

Results also show a strong peak-dependent behaviour, that can be explained by multiple factors. The first one is that the hyperpolarization process is metabolite-dependent, which can lead to different polarization levels. The second one is that hyperpolarization is decaying according to T₁ relaxation, which is specific of each signal and of each solvent. The third one is that the dissolution yield is not the same for all metabolites, depending on their solubility in a given solvent. This is the case for arginine, for instance, which is very poorly soluble in MeOD and that we are not able to observe in d-DNP UF experiments recorded in MeOD (as shown in Fig. 3c). Finally, the UF long-range HETCOR provides a peak-specific response factor, as any multi-pulse NMR experiment. With such peak-specific response, absolute quantification would require a calibration or standard additions procedures, as it is already the case for the vast majority of quantitative 2D NMR experiments⁶² and as illustrated very recently in the case of hyperpolarised 1D ¹³C

NMR. Ribay *et al.* showed that the absolute quantification of hyperpolarized natural abundance metabolites in freeze-dried urine samples was possible relying on a standard addition protocol, while retaining a repeatability of the concentration determination below 10%.⁴⁹ In any case, relative quantification of each metabolite across a set of samples remains possible thanks to the good linearity and repeatability of the method, as required for untargeted metabolomics.

While the concentrations reported in Tables 1 and S3 are those in the initial sample placed in the polarizer, the detected concentrations in the NMR tube after dissolution are in average 70 times lower for D₂O dissolutions and 123 times lower for MeOD dissolutions, as calculated by the determination of absolute concentrations in different post-dissolution NMR samples. The dilution factor first arises from the dilution of 200 μL of the sample in the polarizer by the 5 mL of hot solvent and from the metabolite solubility which is about twice higher in D₂O than in MeOD. It highlights both the excellent performance of the NMR detection scheme, which actually detects micromolar concentrations in a single scan at natural ¹³C abundance, but also the strong need to reduce this dilution factor in the future to access lower concentrations. Alternative d-DNP settings are being developed, such as the bullet-DNP method that transfers a bullet containing the previously polarized glassy-matrix that is dissolved only right before detection, in a small compartment above the NMR sample tube, avoiding at the same time strong motion and large dilution of the sample.^{63–65} Another approach could be the use of a liquid-driven transfer,³⁹ that can shorten the transfer time to about 2 seconds, especially in the case of long distances between the polarizer and the NMR detection magnet (up to 10 meters). This system could also help the UF detection, as it further reduces the sample motion in the NMR tube, but at the cost of a higher dilution factor in D₂O of ca. 110.

4. Conclusions

We have shown that d-DNP UF 2D NMR spectroscopy allows to record informative hyperpolarized 2D maps, in a time that is compatible with high-throughput analysis (ca. 20 min per sample). A repeatability of around 10% and a good linearity

were achieved for both MeOD and D₂O as dissolution solvents, which is suitable for complex mixture analysis and for most metabolomics applications. LOQ values of a few mM can be achieved with the d-DNP UF 2D NMR workflow, which can be promising for the study of concentrated metabolite mixtures, such as extracts. Ongoing efforts to implement less turbulent transfer and reduce the stabilization time and the dilution factor will be key to apply the method to more diluted samples such as biofluids, and could also allow applying more sensitive homonuclear ultrafast 2D pulse sequences after dissolution. On the detection side, it has already been shown that using a triple-axis can efficiently reduce the strong artefact occurrences, by performing the coherence selection on an orthogonal axis to the encoding gradient or even to perform spatial encoding on an axis orthogonal to residual motion. Overall, UF 2D NMR appears as an efficient method to facilitate the assignment and integration of metabolite signals in hyperpolarized complex mixtures.

Author Contributions

All the authors: conceptualisation, methodology, writing – review & editing. CP, VR, AD, JM, BC: investigation, data curation, formal analysis, validation. CP, JND, PG: visualisation, writing – original draft; JND, PG: funding acquisition, supervision. PG: project administration.

Conflicts of interest

There are no conflicts to declare.

Acknowledgements

This work has received funding from the European Research Council under the European Union's Horizon 2020 research and innovation program (grant agreements no 814747/SUMMIT and 801774/DINAMIX) and the Region Pays de la Loire (ConnectTalent/HPNMR). Authors from CEISAM acknowledge the French National Infrastructure for Metabolomics and Fluxomics MetaboHUB-ANR-11-INBS-0010 (www.metabohub.fr) and the Corsaire metabolomics core facility (Biogenouest). This work includes NMR experiments carried out on the CEISAM NMR platform.

Notes and references

- 1 A.-H. Emwas, R. Roy, R. T. McKay, L. Tenori, E. Saccenti, G. A. N. Gowda, D. Rafferty, F. Alahmari, L. Jaremko, M. Jaremko and D. S. Wishart, *Metabolites*, 2019, **9**, 123.
- 2 J. W. Allwood, A. Williams, H. Uthe, N. M. van Dam, L. A. J. Mur, M. R. Grant and P. Pétriaccq, *Metabolites*, 2021, **11**, 558.
- 3 J. G. Bundy, M. P. Davey and M. R. Viant, *Metabolomics*, 2009, **5**, 3–21.
- 4 T. M. O'Connell, *Metabolites*, 2020, **10**, 120.
- 5 L. Puchades-Carrasco and A. Pineda-Lucena, *Curr. Top. Med. Chem.*, DOI:10.2174/1568026617666170707120034.
- 6 E. Riekeberg and R. Powers, *F1000Research*, 2017, **6**, 1148.

- 7 X. Liu and J. W. Locasale, *Trends Biochem. Sci.*, 2017, **42**, 274–284.
- 8 Y. Ben-Tal, P. J. Boaler, H. J. A. Dale, R. E. Dooley, N. A. Fohn, Y. Gao, A. García-Domínguez, K. M. Grant, A. M. R. Hall, H. L. D. Hayes, M. M. Kucharski, R. Wei and G. C. Lloyd-Jones, *Prog. Nucl. Magn. Reson. Spectrosc.*, 2022, **129**, 28–106.
- 9 D. A. Foley, J. Wang, B. Maranzano, M. T. Zell, B. L. Marquez, Y. Xiang and G. L. Reid, *Anal. Chem.*, 2013, **85**, 8928–8932.
- 10 T. C. Malig, J. D. B. Koenig, H. Situ, N. K. Chehal, P. G. Hultin and J. E. Hein, *React. Chem. Eng.*, 2017, **2**, 309–314.
- 11 P. Renzi, J. Hioe and R. M. Gschwind, *Acc. Chem. Res.*, 2017, **50**, 2936–2948.
- 12 C. Lima, H. Muhamadali and R. Goodacre, *Annu. Rev. Anal. Chem.*, 2021, **14**, 323–345.
- 13 J. Martens, G. Berden, R. E. van Outersterp, L. A. J. Kluijtmans, U. F. Engelke, C. D. M. van Karnebeek, R. A. Wevers and J. Oomens, *Sci. Rep.*, 2017, **7**, 3363.
- 14 J.-L. Ren, A.-H. Zhang, L. Kong and X.-J. Wang, *RSC Adv.*, 2018, **8**, 22335–22350.
- 15 J.-N. Dumez, *Chem. Commun.*, 2022, **58**, 13855–13872.
- 16 J. Marchand, E. Martineau, Y. Guitton, G. Dervilly-Pinel and P. Giraudeau, *Curr. Opin. Biotechnol.*, 2017, **43**, 49–55.
- 17 A. L. Guennec, P. Giraudeau and S. Caldarelli, *Anal. Chem.*, 2014, **86**, 5946–5954.
- 18 B. Féraud, B. Govaerts, M. Verleysen and P. de Tullio, *Metabolomics*, 2015, **11**, 1756–1768.
- 19 V. Sans, L. Porwol, V. Dragone and L. Cronin, *Chem. Sci.*, 2015, **6**, 1258–1264.
- 20 M. P. Schätzlein, J. Becker, D. Schulze-Sünninghausen, A. Pineda-Lucena, J. R. Herance and B. Luy, *Anal. Bioanal. Chem.*, 2018, **410**, 2793–2804.
- 21 E. Kupče and R. Freeman, *Magn. Reson. Chem.*, 2007, **45**, 2–4.
- 22 C. Mauve, S. Khelifi, F. Gilard, G. Mouille and J. Farjon, *Chem. Commun.*, 2016, **52**, 6142–6145.
- 23 A. Le Guennec, J.-N. Dumez, P. Giraudeau and S. Caldarelli, *Magn. Reson. Chem.*, 2015, **53**, 913–920.
- 24 J. Marchand, E. Martineau, Y. Guitton, B. Le Bizec, G. Dervilly-Pinel and P. Giraudeau, *Metabolomics*, 2018, **14**, 60.
- 25 C. Ludwig, D. G. Ward, A. Martin, M. R. Viant, T. Ismail, P. J. Johnson, M. J. O. Wakelam and U. L. Günther, *Magn. Reson. Chem.*, 2009, **47**, S68–S73.
- 26 B. Gouilleux, J. Marchand, B. Charrier, G. S. Remaud and P. Giraudeau, *Food Chem.*, 2018, **244**, 153–158.
- 27 A. Le Guennec, I. Tea, I. Antheaume, E. Martineau, B. Charrier, M. Pathan, S. Akoka and P. Giraudeau, *Anal. Chem.*, 2012, **84**, 10831–10837.
- 28 R. Fraser, F. P. J. T. Rutjes, M. C. Feiters and M. Tessari, *Acc. Chem. Res.*, 2022, **55**, 1832–1844.
- 29 K. Ausmees, N. Reimets and I. Reile, *Molecules*, 2022, **27**, 802.
- 30 L. S. Lloyd, R. W. Adams, M. Bernstein, S. Coombes, S. B. Duckett, G. G. R. Green, Richard. J. Lewis, R. E. Mewis and C. J. Sleigh, *J. Am. Chem. Soc.*, 2012, **134**, 12904–12907.
- 31 I. Reile, R. L. E. G. Aspers, J.-M. Tyburn, J. G. Kempf, M. C. Feiters, F. P. J. T. Rutjes and M. Tessari, *Angew. Chem. Int. Ed.*, 2017, **56**, 9174–9177.
- 32 L. Sellies, I. Reile, R. L. E. G. Aspers, M. C. Feiters, F. P. J. T. Rutjes and M. Tessari, *Chem. Commun.*, 2019, **55**, 7235–7238.
- 33 N. Reimets, K. Ausmees, S. Vija and I. Reile, *Anal. Chem.*, 2021, **93**, 9480–9485.
- 34 B. Plainchont, P. Berruyer, J.-N. Dumez, S. Jannin and P. Giraudeau, *Anal. Chem.*, 2018, **90**, 3639–3650.
- 35 J. H. Ardenkjær-Larsen, B. Fridlund, A. Gram, G. Hansson, L. Hansson, M. H. Lerche, R. Servin, M. Thaning and K. Golman, *Proc. Natl. Acad. Sci.*, 2003, **100**, 10158–10163.
- 36 A. Bornet, R. Melzi, A. J. Perez Linde, P. Hautle, B. van den Brandt, S. Jannin and G. Bodenhausen, *J. Phys. Chem. Lett.*, 2013, **4**, 111–114.

- 37 S. J. Elliott, Q. Stern, M. Ceillier, T. El Daraï, S. F. Cousin, O. Cala and S. Jannin, *Prog. Nucl. Magn. Reson. Spectrosc.*, 2021, **126–127**, 59–100.
- 38 S. Jannin, J.-N. Dumez, P. Giraudeau and D. Kurzbach, *J. Magn. Reson.*, 2019, **305**, 41–50.
- 39 M. Ceillier, O. Cala, T. El Daraï, S. F. Cousin, Q. Stern, S. Guibert, S. J. Elliott, A. Bornet, B. Vuichoud, J. Milani, C. Pages, D. Eshchenko, J. G. Kempf, C. Jose, S. A. Lambert and S. Jannin, *J. Magn. Reson. Open*, 2021, **8–9**, 100017.
- 40 J. Granwehr, R. Panek, J. Leggett and W. Köckenberger, *J. Chem. Phys.*, 2010, **132**, 244507.
- 41 H.-Y. Chen and C. Hilty, *ChemPhysChem*, 2015, **16**, 2646–2652.
- 42 S. Katsikis, I. Marin-Montesinos, M. Pons, C. Ludwig and U. L. Günther, *Appl. Magn. Reson.*, 2015, **46**, 723–729.
- 43 A. Dey, B. Charrier, K. Lemaitre, V. Ribay, D. Eshchenko, M. Schnell, R. Melzi, Q. Stern, S. F. Cousin, J. G. Kempf, S. Jannin, J.-N. Dumez and P. Giraudeau, *Magn. Reson.*, 2022, **3**, 183–202.
- 44 A. Bornet, M. Maucourt, C. Deborde, D. Jacob, J. Milani, B. Vuichoud, X. Ji, J.-N. Dumez, A. Moing, G. Bodenhausen, S. Jannin and P. Giraudeau, *Anal. Chem.*, 2016, **88**, 6179–6183.
- 45 M. H. Lerche, D. Yigit, A. B. Frahm, J. H. Ardenkjær-Larsen, R. M. Malinowski and P. R. Jensen, *Anal. Chem.*, 2018, **90**, 674–678.
- 46 A. B. Frahm, P. R. Jensen, J. H. Ardenkjær-Larsen, D. Yigit and M. H. Lerche, *J. Magn. Reson.*, 2020, **316**, 106750.
- 47 A. B. Frahm, D. Hill, S. Katsikis, T. Andreassen, J. H. Ardenkjær-Larsen, T. F. Bathen, S. A. Moestue, P. R. Jensen and M. H. Lerche, *Talanta*, 2021, **235**, 122812.
- 48 A. Dey, B. Charrier, E. Martineau, C. Deborde, E. Gandriau, A. Moing, D. Jacob, D. Eshchenko, M. Schnell, R. Melzi, D. Kurzbach, M. Ceillier, Q. Chappuis, S. F. Cousin, J. G. Kempf, S. Jannin, J.-N. Dumez and P. Giraudeau, *Anal. Chem.*, 2020, **92**, 14867–14871.
- 49 V. Ribay, A. Dey, B. Charrier, C. Praud, J. Mandral, J.-N. Dumez, M. P. M. Letertre and P. Giraudeau, *Angew. Chem. Int. Ed.*, 2023, **62**, e202302110.
- 50 S. Katsikis, I. Marin-Montesinos, C. Ludwig and U. L. Günther, *J. Magn. Reson.*, 2019, **305**, 175–179.
- 51 L. Frydman, T. Scherf and A. Lupulescu, *Proc. Natl. Acad. Sci.*, 2002, **99**, 15858–15862.
- 52 L. Frydman and D. Blazina, *Nat. Phys.*, 2007, **3**, 415–419.
- 53 M. Mishkovsky and L. Frydman, *ChemPhysChem*, 2008, **9**, 2340–2348.
- 54 P. Giraudeau, Y. Shrot and L. Frydman, *J. Am. Chem. Soc.*, 2009, **131**, 13902–13903.
- 55 J.-N. Dumez, J. Milani, B. Vuichoud, A. Bornet, J. Lalande-Martin, I. Tea, M. Yon, M. Maucourt, C. Deborde, A. Moing, L. Frydman, G. Bodenhausen, S. Jannin and P. Giraudeau, *Analyst*, 2015, **140**, 5860–5863.
- 56 A. Singh, A. Dubey, S. K. Adiga and H. S. Atreya, *J. Magn. Reson.*, 2018, **286**, 10–16.
- 57 R. Panek, J. Granwehr, J. Leggett and W. Köckenberger, *Phys. Chem. Chem. Phys.*, 2010, **12**, 5771–5778.
- 58 K. Singh, C. Jacquemmoz, P. Giraudeau, L. Frydman and J.-N. Dumez, *Chem. Commun.*, 2021, **57**, 8035–8038.
- 59 J. Furrer, *Chem. Commun.*, 2010, **46**, 3396–3398.
- 60 C. Lhoste, B. Lorandel, C. Praud, A. Marchand, R. Mishra, A. Dey, A. Bernard, J.-N. Dumez and P. Giraudeau, *Prog. Nucl. Magn. Reson. Spectrosc.*, 2022, **130–131**, 1–46.
- 61 C. Canlet, C. Deborde, E. Cahoreau, G. Da Costa, R. Gautier, D. Jacob, C. Jousse, M. Lacaze, I. Le Mao, E. Martineau, L. Peyriga, T. Richard, V. Silvestre, M. Traïkia, A. Moing and P. Giraudeau, *Metabolomics*, 2023, **19**, 65.
- 62 P. Giraudeau, *Chem. Commun.*, 2023, **59**, 6627–6642.
- 63 K. Kouřil, H. Kouřilová, S. Bartram, M. H. Levitt and B. Meier, *Nat. Commun.*, 2019, **10**, 1733.
- 64 S. Van Meerten, F. Van Zelst, K. Tijssen and A. Kentgens, *Anal. Chem.*, 2020, **92**, 13010–13016.
- 65 K. Kouřil, M. Gramberg, M. Jurkutat, H. Kouřilová and B. Meier, *Magn. Reson.*, 2021, **2**, 815–825.